

Measurement of neutron beam spot distribution using a Micromegas detector for the Back-n white neutron facility at China Spallation Neutron Source

Binbin Qi^{a,b,1}, Yang Li^{c,d,1}, Danyang Zhu^{a,b}, Zhiyong Zhang^{a,b,*}, Ruirui Fan^{e,c,d,*}, Jiang Pan^{a,b}, Jianxin Feng^{a,b}, Chengming Liu^{a,b}, Changqing Feng^{a,b}, Jianbei Liu^{a,b}, Ming Shao^{a,b}, Yi Zhou^{a,b}, Yanfeng Wang^{c,d}, Han Yi^{c,d}, Qi An^{a,b}, Huaiyong Bai^f, Jie Bao^g, Ping Cao^{a,b}, Qiping Chen^h, Yonghao Chen^{c,d}, Pinjing Chengⁱ, Zengqi Cui^f, Minhao Gu^{e,c}, Fengqin Guo^{c,d}, Changcai Han^j, Zijie Han^h, Guozhu He^g, Yongcheng He^{c,d}, Yuefeng He^l, Hanxiong Huang^g, Weiling Huang^{c,d}, Xiru Huang^{a,b}, Xiaolu Ji^{e,c}, Xuyang Ji^{a,k}, Haoyu Jiang^f, Wei Jiang^{c,d}, Hantao Jing^{c,d}, Ling Kang^{c,d}, Mingtao Kang^{c,d}, Bo Li^{c,d}, Lun Li^{c,d}, Qiang Li^{c,d}, Xiao Li^{c,d}, Yang Li^{e,c}, Rong Liu^h, Shubin Liu^{a,b}, Xingyan Liu^h, Guangyuan Luan^g, Yinglin Ma^{c,d}, Changjun Ning^{c,d}, Jie Ren^g, Xichao Ruan^g, Zhaojun Song^j, Hong Sun^{c,d}, Xiaoyang Sun^{c,d}, Zhijia Sun^{e,c,d}, Zhixin Tan^{c,d}, Hongqing Tang^g, Jingyu Tang^{c,d}, Pengcheng Wang^{c,d}, Qi Wang^g, Taofeng Wang^l, Zhaohui Wang^g, Zheng Wang^{c,d}, Jie Wen^h, Zhongwei Wen^h, Qingbiao Wu^{c,d}, Xiaoguang Wu^g, Xuan Wu^{c,d}, Likun Xie^{a,k}, Yiwei Yang^h, Li Yu^{c,d}, Tao Yu^{a,b}, Yongji Yu^{c,d}, Guohui Zhang^f, Jing Zhang^{c,d}, Linhao Zhang^{c,d}, Liying Zhang^{a,c,d}, Qingming Zhang^m, Qiwei Zhang^g, Xianpeng Zhang^j, Yuliang Zhang^{c,d}, Yingtan Zhao^m, Liang Zhou^{c,d}, Zuying Zhou^g, Kejun Zhu^{e,c}, Peng Zhu^{c,d}

^a*State Key Laboratory of Particle Detection and Electronics, University of Science and Technology of China, Hefei 230026, China*

^b*Department of Modern Physics, University of Science and Technology of China, Hefei 230026, China*

^c*Institute of High Energy Physics, Chinese Academy of Sciences, Beijing 100049, China*

^d*Spallation Neutron Source Science Center, Dongguan 523803, China*

^e*State Key Laboratory of Particle Detection and Electronics, Institute of High Energy Physics, Chinese Academy of Sciences, Beijing 100049, China*

^f*State Key Laboratory of Nuclear Physics and Technology, School of Physics, Peking University, Beijing 100871, China*

^g*Key Laboratory of Nuclear Data, China Institute of Atomic Energy, Beijing 102413, China*

^h*Institute of Nuclear Physics and Chemistry, China Academy of Engineering Physics, Mianyang 621900, China*

ⁱ*University of South China, Hengyang 421001, China*

^j*Northwest Institute of Nuclear Technology, Xian 710024, China*

^k*Department of Engineering and Applied Physics, University of Science and Technology of China, Hefei 230026, China*

^l*School of Physics, Beihang University 100083, China*

^m*Xian Jiaotong University, Xian 710049, China*

*Corresponding author.

Email addresses: zhzhyl@ustc.edu.cn (Zhiyong Zhang), fanrr@ihep.ac.cn (Ruirui Fan)

¹Co-first author. These authors contributed equally to this work.

Abstract

The Back-n white neutron beam line, which uses back-streaming white neutrons from the spallation target of China Spallation Neutron Source, is useful for nuclear data measurements. A Micromegas-based neutron detector with two variants is developed to measure the beam spot distribution for this beam line. In this article, the design, fabrication, and characterization of the detector are described. The results of the detector performance tests are presented, which include the relative electron transparency, the gain and the gain uniformity, and the neutron detection capability. The first measurement result of the Back-n neutron beam spot distribution is also presented.

Keywords: Micromegas detector, neutron beam spot distribution, white neutron beam, spallation neutron source

1. Introduction

The neutron beam line using back-streaming white neutrons (Back-n) [1–3] at China Spallation Neutron Source (CSNS) [4, 5] was built and commissioned in 2018. This beam line is called the Back-n white neutron beam line or simply Back-n. Back-n delivers an intense neutron flux up to $\sim 10^7 \text{ cm}^{-2} \text{ s}^{-1}$ at a distance of 55 m from the spallation target at 100 kW proton beam power, and the neutrons span many orders of magnitude in energy, from 0.5 eV to several hundreds of MeV.

Equipped with several dedicated spectrometers, Back-n is a useful facility for nuclear data measurements, providing critical data for various typical research such as the design of nuclear energy facilities, nuclear astrophysics research, and improving the current nuclear databases which have very wide applications. Measurements of the neutron beam properties, e.g., the spot distribution, the intensity, and the energy spectrum of the neutron beam, are the basic requirement for this kind of facilities. Thanks to the good two-dimensional (2D) spatial resolution and fast timing capability of the Micromegas (micro-mesh

gaseous structure) detector [6, 7], it can be used for a quasi-online measurement of neutron beam spot distribution or profile [8] at the Back-n white neutron facility.

Micromegas detectors (MMDs) have been widely used in nuclear and particle physics including rare-event searches [9, 10] and neutron detection [11]. In this article, we present the development of an MMD with 2D spatial resolution capability for measuring neutron beam spot distribution. Potentially, it can be used as an online profile monitor for some experiments. For a neutron to be detected, it needs to be converted into charged particles using nuclear reactions. A thin layer deposit of ^{10}B or ^6Li on a thin aluminum foil is used as the neutron converter. The current setup of the MMD, used as a beam profiler at Back-n, sums up the neutron events of the entire energy range, with higher weight on low-energy neutrons due to higher cross sections for both ^{10}B and ^6Li . However, it is feasible to reconstruct the energy dependence of the Back-n neutron flux with the MMD, because (a) the neutron time of flight (TOF) from the spallation target to the detector can be measured and (b) the neutron cross sections of ^{10}B and ^6Li are standard below 1 MeV or they can be precisely measured in a wide energy range at Back-n. This is planned as part of the detector upgrades in the future.

2. The Micromegas detector

2.1. Detector design and setup

Figure 1 shows the MMD of this work. The neutron converter is prior to the drift region (i.e., the region between cathode and mesh). The mesh-anode amplification region is manufactured with the thermal bonding technique (see Refs. [12, 13] for detailed description of the manufacturing process). With this technique, each side of the readout PCB is attached with a metallic mesh to form the avalanche gap (the amplification region where electron avalanches occur), thus a back-to-back structure is obtained, as shown in Fig. 2. The mesh and the anode plane are separated by insulating pillars. Each pillar has a cylindrical

shape of 2 mm in diameter. These two avalanche structures are able to work simultaneously for a higher detection efficiency. Meanwhile, the MMD can also be used in the redundant working mode, where only one avalanche gap is working and the other provides redundancy for the measurement. The avalanche gap and the drift gap are 100 μm and 5 mm, respectively. The total active area of the MMD is 90 mm \times 90 mm.

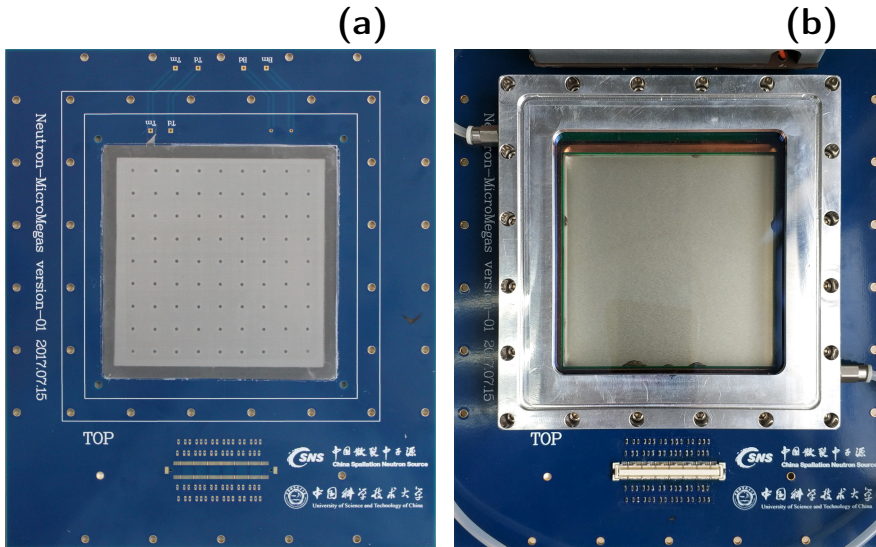


Figure 1: Micromegas fabrication process. (a) The mesh after thermocompression bonding. An array of cylindrical pillars are visible, which hold the mesh and ensure a constant distance between the mesh and the PCB. (b) The detector chamber.

Since the 2D position information of the particle hits is required for the neutron beam monitoring, a 2D readout structure has been designed and built for the MMD (see Fig. 3) to reconstruct the 2D position using strip coincidences. This readout structure allows a better determination of the two coordinates of the position from the charge produced in the amplification volume and induced on the anode strips. A special readout PCB was designed and adapted to the 2D readout strips shown in Fig. 3. Square copper pads, each with dimensions of 1.06 mm \times 1.06 mm, are densely arranged on the surface of the readout PCB,

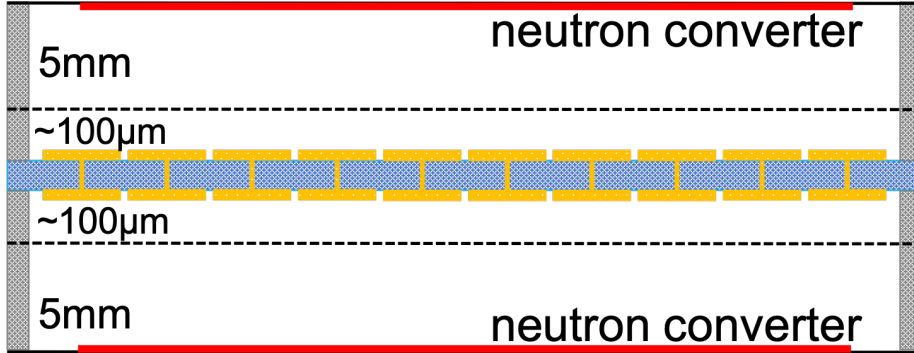


Figure 2: Schematic of the Micromegas with back-to-back double-avalanche structure. The mesh (dashed line) separates the 5 mm drift gap from the 100 μm avalanche gap. Each of the XY readout strips is independently connected to the central board.

with a bevel of 45°. The pads are interconnected by two groups of wires in orthogonal directions, such that symmetrical XY strip readouts are formed, with 64 strips (1.5 mm pitch) in each direction. Each readout strip is capacitively coupled into a charge amplifier, corresponding to one readout channel. The goals of this 2D readout scheme are (a) to mitigate the unequal charge sharing between the two strip layers that occurs in standard XY detectors and (b) to minimize the material budget of the detector.

Two detector units (MMD-1 and MMD-2) with different anode designs were fabricated. For MMD-1, copper anode is used; for MMD-2, resistive anode with germanium coating is used. The copper-anode MMD-1 is easier to fabricate despite the lower gain than the resistive-anode MMD-2. The resistive layer of MMD-2 protects the detector from the sparking caused by intense ionization of ions.

2.2. *Front-end electronics*

A dedicated front-end electronics (FEE) system based on the AGET ASIC chip [14] was developed to process the MMD strip signals that are read out independently. Each AGET chip features 64 analog channels. In total, two

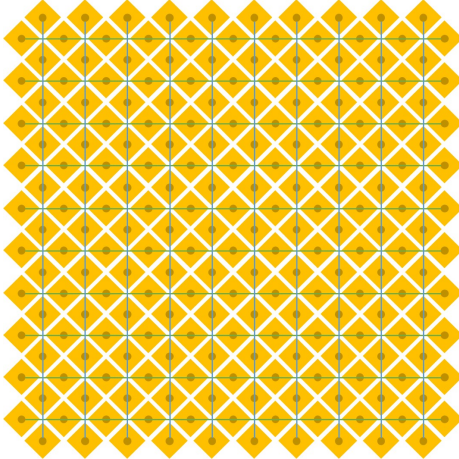


Figure 3: Schematics of the 2D readout structure. The squares represent the copper pads that cover the surface of readout PCB. The pads are interconnected by two groups of wires (represented by the horizontal and vertical lines) to the readout electronics through conductive vias in two extra layers added underneath the readout PCB surface, such that orthogonal strip readouts are formed.

AGET chips with 128 channels are used. Each channel records 512 sampling points with adjustable sampling frequency from 3 MHz to 100 MHz, which meets the basic requirement for the signal data processing. The raw signal of each readout channel is presented as a 12-bit ADC value.

2.3. Neutron converter

The neutrons are indirectly detected by the detection of the secondary charged particles produced in the interaction of neutrons with a target (neutron converter) plated on the drift electrode. Two types of neutron converters with well-known cross sections (${}^6\text{Li}$ and ${}^{10}\text{B}$) are used. For MMD-2, ${}^6\text{Li}$ is used, producing a triton and an alpha particle via the ${}^6\text{Li}(n, t){}^4\text{He}$ reaction [15]:



Figure 4(a) shows a layer of ${}^6\text{LiF}$ with a diameter of 6 cm deposited on the bottom surface of a thin aluminum film (the drift electrode) as the neutron

converter. For MMD-1, ^{10}B is used, with the $^{10}\text{B}(n, \alpha)^7\text{Li}$ reaction:



or



for which the branching fractions are 94% and 6%, respectively. The energies of the reaction products are shown in Eqs. (1), (2), and (3) for the cases of thermal neutrons. Figure 4(b) shows a layer of natural ^{10}B (with the thickness of 0.1 μm and dimensions of 9 cm \times 9 cm) deposited over the entire bottom surface of the aluminum drift electrode as the neutron converter. In addition, a boron layer of 1 μm thick was also produced and used for MMD-2 for performance comparison.

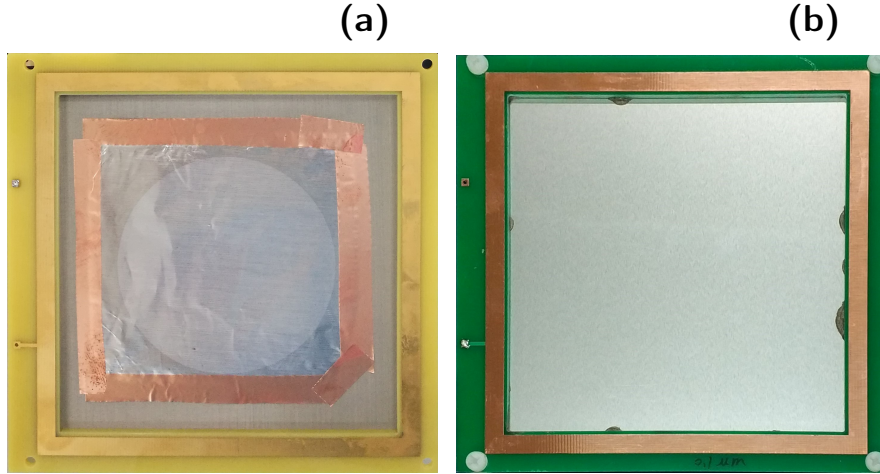


Figure 4: (a) The neutron converter for MMD-1: a 6 cm diameter ^6LiF layer coated on the bottom surface of a thin aluminum film (used as the drift electrode). (b) The neutron converter for MMD-2: a 0.1 μm thick layer of natural ^{10}B coated on the entire bottom surface of the aluminum drift electrode (9 cm \times 9 cm).

3. Performance tests with X-rays and α -rays

3.1. Detector characterization with X-rays

An ^{55}Fe X-ray source (5.9 keV) was used to test the detector performance, including the relative electron transparency, the gain, and the gain uniformity. The detector chamber was filled with a gas mixture of 93% argon (Ar) and 7% CO_2 at atmospheric pressure. The signal from the mesh was amplified by a charge sensitive preamplifier and a shaping amplifier, and subsequently digitized by a multi-channel analyzer.

The relative electron transparency was found to reach a plateau when the ratio of the electric fields in the amplification region and in the drift region ($E_{\text{mesh}}/E_{\text{drift}}$) is greater than 150. Therefore in the subsequent performance studies, the $E_{\text{mesh}}/E_{\text{drift}}$ ratio was fixed to 160 for a maximal electron transparency. The measured gains of MMD-1 and MMD-2 are shown in Fig. 5. One can see, the highest gains of MMD-1 and MMD-2 (with E_{mesh} below the breakdown voltage) are about 20 000 and 3000, respectively, which meet the basic requirement for the detection of the charged particles from the neutron interaction. The gain uniformity was calculated as the standard deviation of the gains measured at different positions of the detector active area normalized to the mean. In total, the gains were measured at nine different places with a scanning step of 3 cm. The uniformities of the top and bottom converters of MMD-1 were measured to be 13% and 22%, respectively. By optimizing the thermal bonding technique, the top and bottom uniformities of MMD-2 were improved to 9% and 7%, respectively.

3.2. Position reconstruction test with an α source

The reconstruction of the neutron interaction position is a crucial part of the neutron beam profiling with MMD. Position reconstruction algorithms were tested with an ^{241}Am source which radiates α rays, simulating the reaction products from the neutron interaction, i.e., the $^6\text{Li}(n, t)^4\text{He}$ or $^{10}\text{B}(n, \alpha)^7\text{Li}$ reaction. As shown in Fig. 6, the \sim 5.4 MeV α rays from the ^{241}Am source were

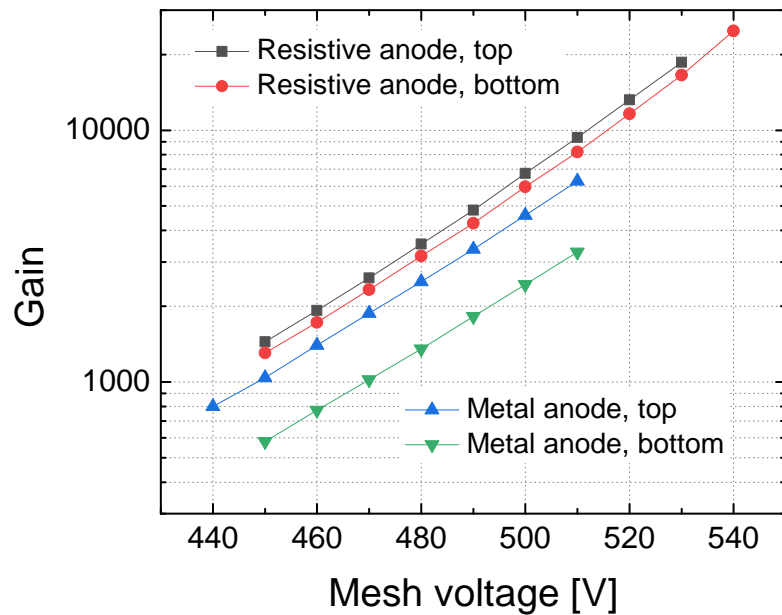


Figure 5: Measured gains of MMD-1 (squares and circles) and MMD-2 (upward- and downward-pointing triangles) as a function of the voltage applied to the mesh with the $E_{\text{mesh}}/E_{\text{drift}}$ ratio fixed to 160.

collimated by a 1 mm diameter pinhole on the drift cathode, and subsequently attenuated by the air and a $\sim 10 \mu\text{m}$ thick plastic film before entering the drift region. Only one side of the MMD was operating during this test.

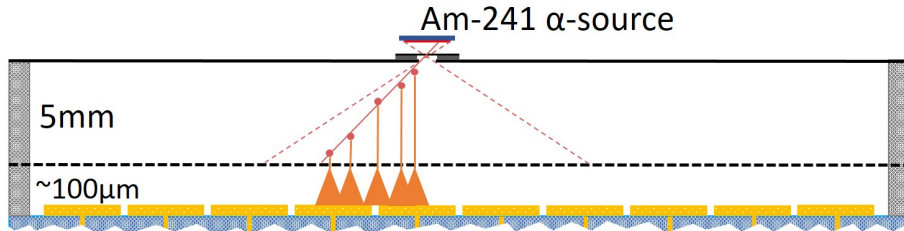


Figure 6: Schematic of the setup for the position reconstruction test with the ^{241}Am α source.

Two different algorithms for the hit position reconstruction were studied: (a) the charge centroid method, which reconstructs the hit position as the average of the strip position weighted by the strip charge, and (b) the micro time projection chamber (μTPC) method [16–18], which exploits the ability of the MMD to operate as a μTPC , measures the (relative) arrival time of ionization charge on the strip, and takes the latest strip as an estimate of the neutron interaction position in the converter. In principle, the centroid method is accurate for the reconstruction of interaction position of perpendicular neutron beams, but the resolution deteriorates with increasing incident angle, since the signal extends over a larger number of strips. By using the μTPC method, the origin of the primary ionization in the drift gap can be determined, which is a more precise estimate of the neutron interaction position than the charge centroid. Since the peaking time of the FEE can be as short as 70 ns, it allows a simultaneous and independent recording of the time information of the strips. Figure 7 shows the waveforms of the raw signals from four consecutive strips. As can be seen, the time differences between adjacent strips are evident.

In order to compare the performance of these two algorithms, the α events are required to have at least two fired strips. Figure 8 shows the two coordinates

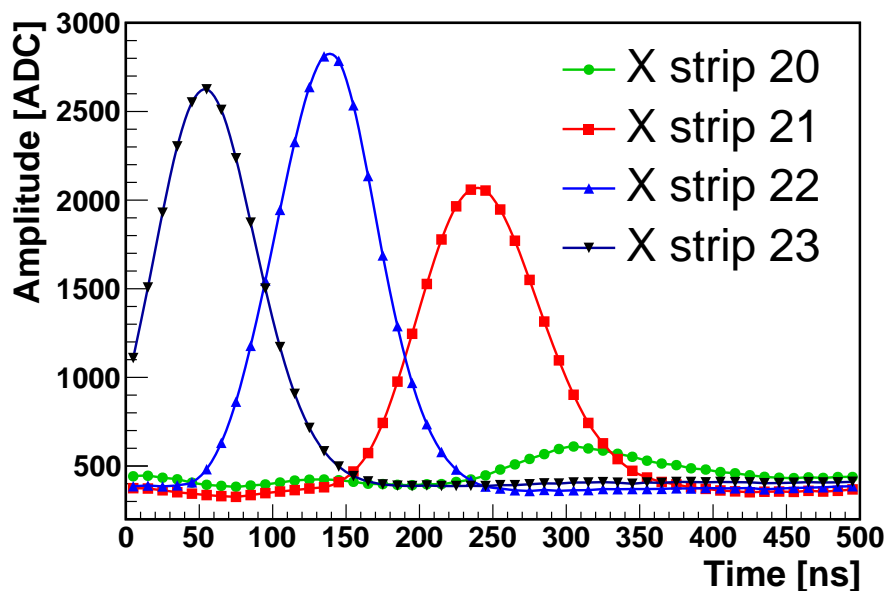


Figure 7: Raw signal waveforms from four consecutive readout strips recorded in an α event. The sampling frequency is 100 MHz.

of the position where the α rays exiting the pinhole collimator reconstructed by these two methods, along with the 1D projections. The distribution of the reconstructed position obtained from the μ TPC method has a much narrower width than that from the charge centroid method, indicating a better spatial resolution for the μ TPC method.

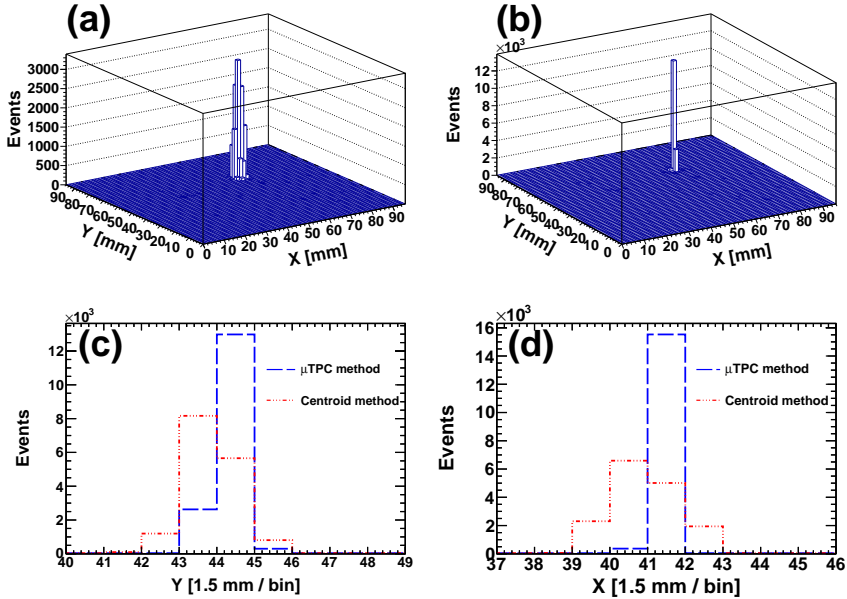


Figure 8: Distributions of the reconstructed position using (a) the charge centroid method and (b) the μ TPC method, and their 1D projections to (c) the Y-axis and (d) the X-axis.

4. Neutron beam spot distribution measurement

4.1. Neutron beam spot distribution measurement with an Am-Be neutron source

The performance of the MMD in the detection of neutrons was tested with an Am-Be neutron source prior to utilizing the Back-n white neutron source. As shown in Fig. 9, MMD-1 with ${}^6\text{Li}$ as the neutron converter was irradiated

with the neutrons from the Am-Be neutron source. In order to moderate these neutrons (with ~ 4.5 MeV mean energy), three 1 cm thick polyethylene layers were placed between the source and MMD-1.

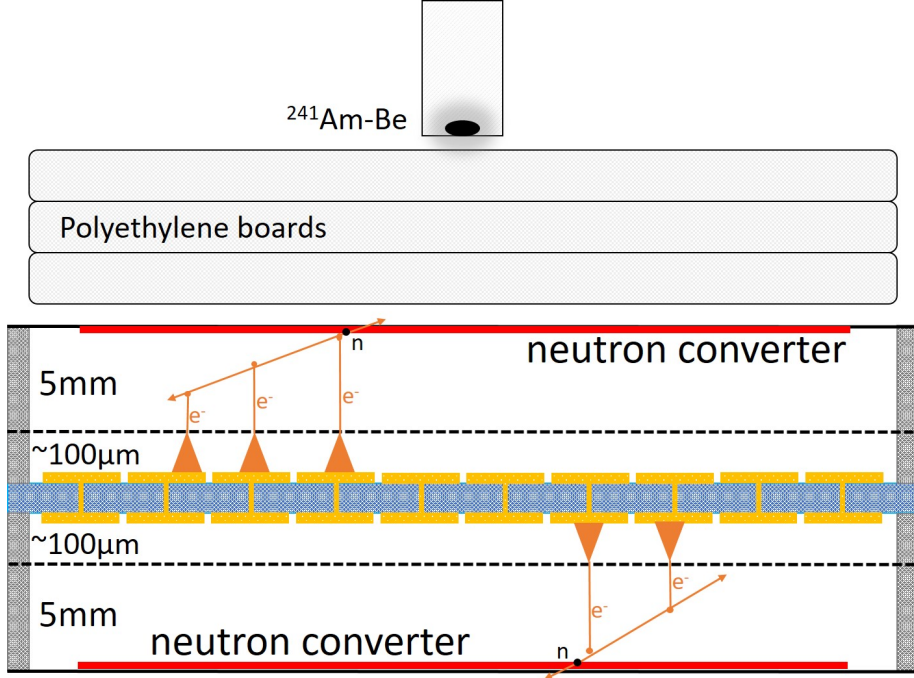


Figure 9: Schematic of the setup for the detector performance test with the Am-Be neutron source.

Figure 10 shows the total charge deposited at the X and Y strips as a function of the total number of those fired strips. Two bands can be seen, corresponding to the two reaction products, a triton and an α particle, from the ${}^6\text{Li}(n, t){}^4\text{He}$ reaction. According to the Bethe-Bloch formula, the ionization energy loss per unit path length is proportional to Z^2 , where Z is the charge of the incident particle. Therefore the α particles have a shorter range than the tritons in the drift region, which results in low strip multiplicities for the α tracks, i.e., the ionization energy deposition of the α tracks only recorded by few strips near the neutron interaction point. Thus, in Fig. 10 the band on the left corresponds to the α particle events, while the band on the right corresponds to the triton

events.

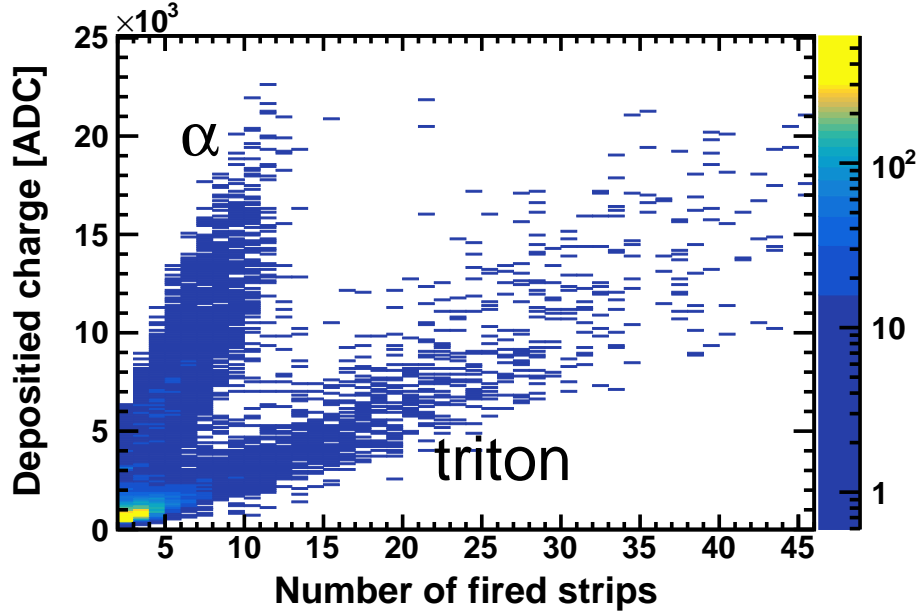


Figure 10: Total charge deposited at the strips as a function of the total number of those fired strips.

The image of the ${}^6\text{LiF}$ neutron converter was reconstructed using the charge centroid method and the μTPC method, as shown in Fig. 11(a) and Fig. 11(b), respectively. Again, a clearer edge of the 2D reconstructed image was obtained by using the μTPC method. This observation is also shown in Fig. 11(c) and Fig. 11(d), where sharper edges of the 1D projections are presented for the μTPC method.

4.2. Neutron beam spot distribution measurement at Back-*n*

The MMD was placed at Back-*n* to study the performance of neutron detection as well as the reconstruction of neutron beam profiles. Along the Back-*n* white neutron beam line there are two experimental halls, Endstation-1 (ES#1) and Endstation-2 (ES#2), which are about 55 m and 76 m away from the spallation target, respectively. The detailed description of Back-*n* is presented in

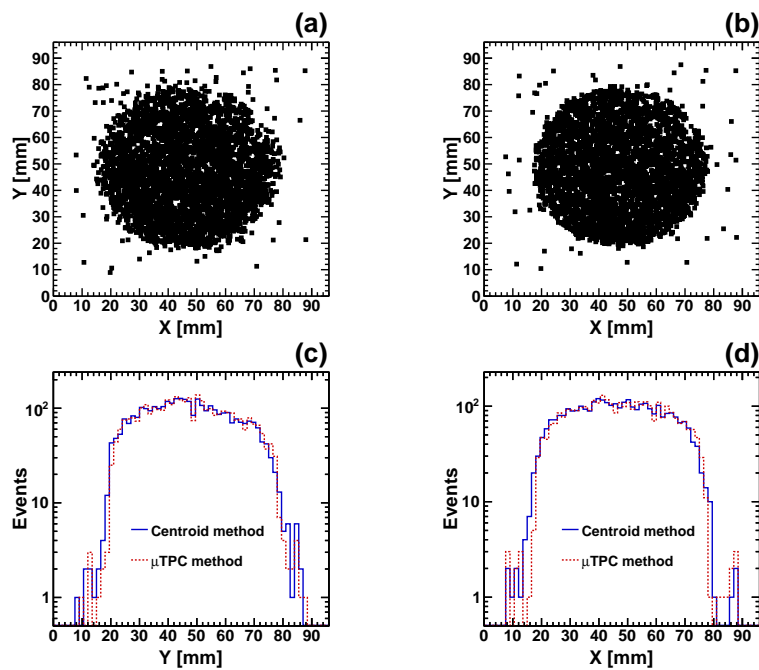


Figure 11: Positions of interaction of the neutrons with the ${}^6\text{LiF}$ layer reconstructed by (a) the charge centroid method and (b) the μ TPC method, and their 1D projections to (c) the Y-axis and (d) the X-axis.

Ref. [19]. The detector was placed at a location in ES#1 which is about 56 m away from the spallation target, and a picture of the experimental setup is shown in Fig. 12. During the data taking period, the CSNS accelerator was operating stably at a repetition rate of 25 Hz and a proton beam power of 20 kW.

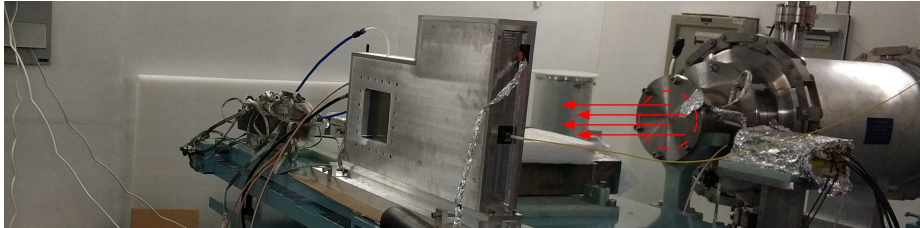


Figure 12: The MMD together with the FEE system was placed in the shielding container made of aluminum, as a neutron beam profiler at Back-n. The arrows represent the incoming neutron beam.

Only one side of the MMD was operating during this measurement. The neutron converter used in this experiment was the 1 μm thick ^{10}B layer on the top surface of the back-to-back structured MMD. Instead of 0.1 μm in many cases, a thicker ^{10}B converter was chosen for a higher neutron reaction rate. The detection gas used was 90% Ar and 10% CO_2 at atmospheric pressure. Limited by the gas flow system at ES#1, a slightly lower fraction of Ar was used compared to the previous tests, which is still within the working range of the detector. The resulting difference in the detector performance is negligible. The dynamic range of the FEE and the sampling frequency of the signal recording were set to 240 fC and 5 MHz, respectively. With 2 ms dead time for the electronics system and 1 μm thick ^{10}B for the converter, the MMD can be used at very high neutron fluxes up to $\sim 10^9 \text{ cm}^{-2} \text{ s}^{-1}$, which corresponds to the Back-n neutron flux at ES#1 at $\sim 10 \text{ MW}$ proton beam power.

The beam spot size at ES#1 is determined by the apertures of the shutter and Collimator-1 of Back-n (see Fig. 6 and Table 1 of Ref. [19]). For this measurement, the configuration of the collimation aperture was set to $\varnothing 50 \text{ mm}$ for the shutter and $\varnothing 50 \text{ mm}$ for Collimator-1, and the corresponding physics

data collection time was about nine hours. Under this configuration, the beam spot size at ES#1 is expected to be about $\varnothing 50$ mm according to the Monte Carlo (MC) simulation study [19]. A dedicated run without beam in the Back-n beam pipe (i.e., the shutter being closed) was taken for ~ 230 s to collect data for pedestal correction.

4.3. Data analysis

4.3.1. Pedestal calculation

Pedestal levels and noise values were calculated for each strip, using the physics run data as well as the pedestal run data for an independent cross-check. For a raw signal waveform recorded by readout channel i for event j , the ADC value of each sampling point, $R_{i,j}$, consists of four components: $R_{i,j} = P_i + CM_j + N_{i,j} + S_{i,j}$, where i is the strip or channel number, j is the event number, and $R_{i,j}$ is an integer between 0 and 4095. The first component is the pedestal level of strip i for n recorded events, which is given by $P_i = (1/n) \sum_{j=1}^n R_{i,j}$. The second component is the common mode of the AGET chip which strip i belongs to, calculated per-event as the mean of $R_{i,j} - P_i$ over 64 channels of the AGET chip. The common mode is the deviation of all the channels of the AGET chip at the same time, mainly originating from the fluctuation of the reference ground of ADCs and differing on an event-by-event basis. The last two components are the intrinsic noise and the signal, respectively. The average intrinsic noise \tilde{N}_i for strip i is calculated as the standard deviation of the common-mode subtracted data.

When using data from a pedestal run to calculate the pedestal, the signal component is negligible. However, when using data from a physics run to calculate the pedestal, the contribution from the signal component (in addition to the pedestal levels) in the raw physics data is nonnegligible. To reduce the contamination from the signal, those $R_{i,j}$ values in the raw waveform satisfying $R_{i,j} - \tilde{P}_{i,j} \geq 3\tilde{N}'_{i,j}$ were excluded in the pedestal calculation, where $\tilde{P}_{i,j}$ and $\tilde{N}'_{i,j}$ are the pedestal and the raw noise (i.e., calculated without the common-mode subtraction), respectively, both calculated up to event j . Most importantly, the

results of the pedestal, common-mode, and noise calculation obtained from the physics run data are consistent with those obtained from the pedestal run data.

4.3.2. Event selection

The first step in the physics data analysis was the pedestal and common-mode subtraction. After that, event selection criteria were applied for the selection of good neutron-induced charged particle events (hereafter referred to as neutron events) and for the rejection of background events or not well recorded neutron events. First, strips with $A_i/\tilde{N}_i < 5$ are invalidated for the event, where A_i is the amplitude of the digitized waveform for strip i after the pedestal and common-mode subtraction. Second, if two or more strips are fired and recorded in an event, those strips should be consecutive, which ensures a continuous ionization of the gas when the charged particle traverses the drift region.

The dominant background to the neutron events comes from the in-beam γ flash produced by the impact of the 1.6 GeV proton beam on the tungsten target, which leads to the emission of a variety of particles other than neutrons, including an intense flux of γ rays that propagates to the Back-n experimental halls through the beam pipe. A large quantity of neutral pions are also produced and decay into γ rays. The use of a bending magnet, about 20 m away from the target, helps to remove the charged particles from the back-streaming neutron beam [19]. Since the recording of the absolute time of the strip signal was not enabled in the readout electronics configuration for this measurement, the rejection of γ -flash background had to rely on the offline analysis. As shown in Fig. 13(a), the multiplicities can be used to discriminate the neutron events and the γ -flash events. Two well separated populations of events are clearly seen. The low (high) multiplicity region, where the X- or Y-strip multiplicities are typically between 1 and 9 (between 10 and 40), corresponds to the neutron (γ -flash) events. This characteristic of the multiplicity distribution is mainly due to that the γ events distribute over the entire beam profile, resulting in a high multiplicity, while for a neutron event, only a few strips around the point of interaction of the neutron with the ^{10}B layer give signals (called fired strips),

resulting in a low multiplicity. Together with the total signal amplitudes of all the fired strips, a clear separation between γ -flash background events and neutron events was obtained, as shown in Fig. 13(b).

4.3.3. Reconstruction of the beam spot distribution

After applying the event selection criteria described above, clean samples of neutron events were obtained for the reconstruction of the beam profile. The μ TPC method was employed for the reconstruction, which uses the central positron of the latest strip as an estimation for the position of the neutron interaction in the converter. The relative time information of each fired strip recorded in an event was determined by performing a fit to the leading edge of the waveform with the Fermi–Dirac function [20]. The fitted time at half height was taken as the arrival time of the strip signal. The fitting range was from 10% to 90% of the maximum height on the leading edge. The strip with the earliest arrival time was taken as reference and the arrival time of adjacent strips was measured relative to it, as shown in Fig. 14. A low sampling frequency (5 MHz) was chosen to ensure a full waveform recording.

Figure 15 shows the reconstructed 2D profile of the Back-n white neutron beam at ES#1. The positions of the pillars (2 mm diameter) are clearly visible. However, these results cannot be directly used to estimate the detector spatial resolution. Placing masks with different shapes like rectangular or circular holes in front of the detector will be part of the future experiment with neutron beams, so that the spatial resolution can be directly estimated. Figures 16(a) and (b) show the 1D projections of the middle Y- and X-slices of the 2D profile onto the X- and Y-axis, respectively, for both data and MC simulation [19]. As can be seen, the measurement and the simulation prediction agree within uncertainties. The reconstructed 2D profile is not circular because the Gaussian proton beam hitting the target does not have circular symmetry, with beam widths of \sim 33 mm in vertical direction and \sim 88 mm in horizontal direction (full width at half maximum).

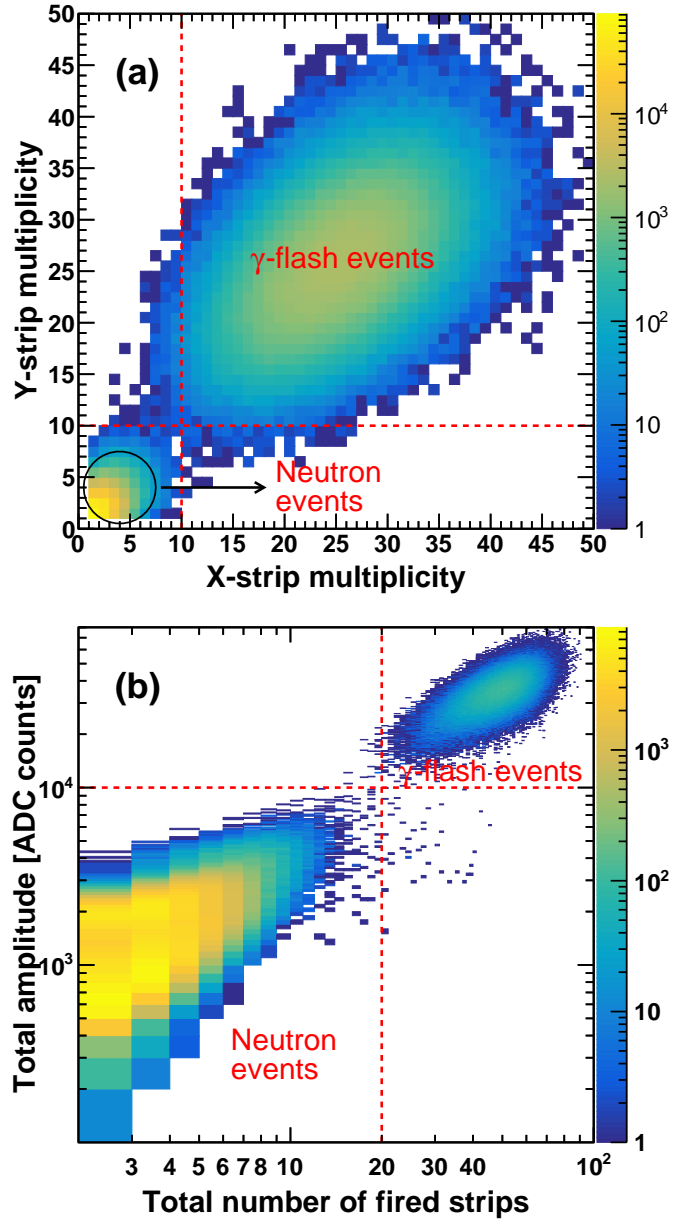


Figure 13: (a) The distribution of the X- and Y-strip multiplicities. (b) Discrimination of γ -flash background events from neutron events by using the total number of fired strips and the sum of the amplitudes of all the fired strips. The dashed lines represent the selection criteria for neutron events. The neutron signal is well separated from the γ -flash background.

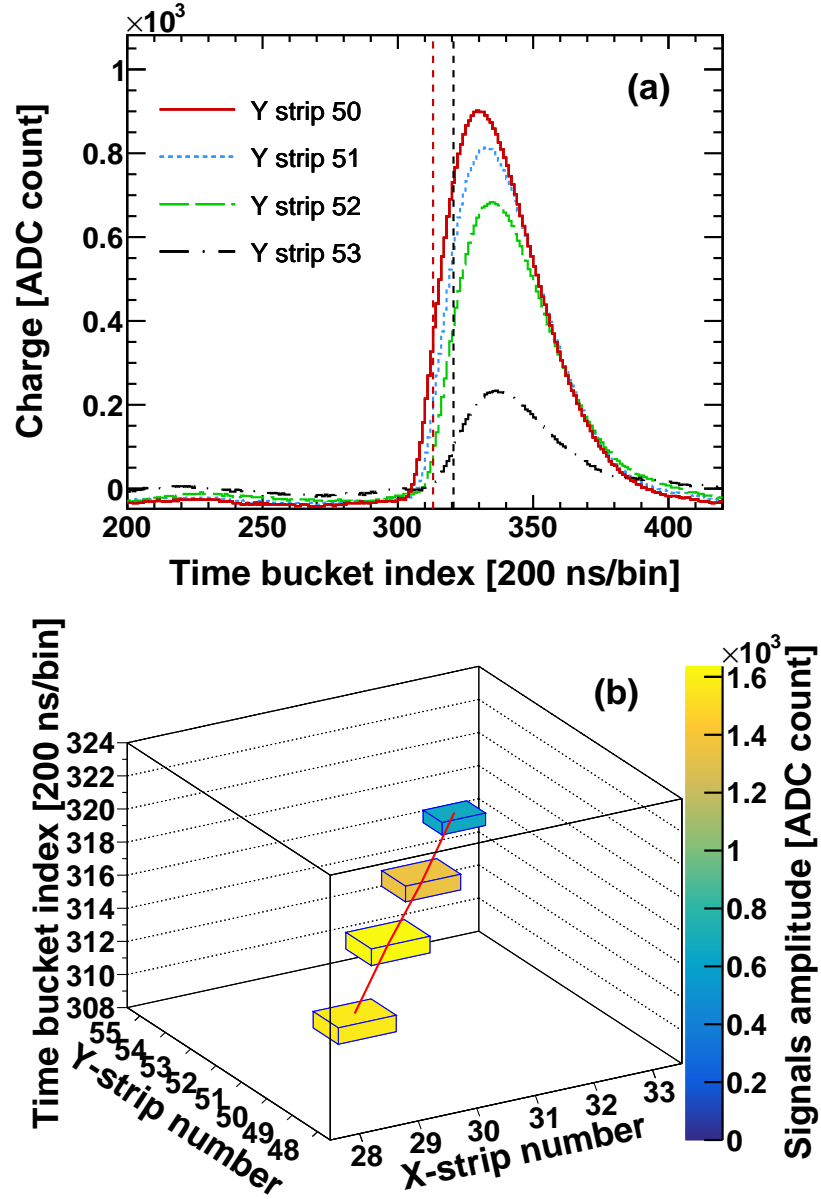


Figure 14: (a) The signal waveforms of four fired Y strips for a charged particle event. The sampling frequency is 5 MHz. The vertical red (black) dashed line represents the time of the earliest (latest) Y strip giving a signal, i.e., Y strip 50 (53). (b) The charges collected by four consecutive X and Y strips along the charged particle trajectory in the gas, represented by the boxes. The color code indicates the sum of X- and Y-strip signal amplitudes in units of [ADC counts].

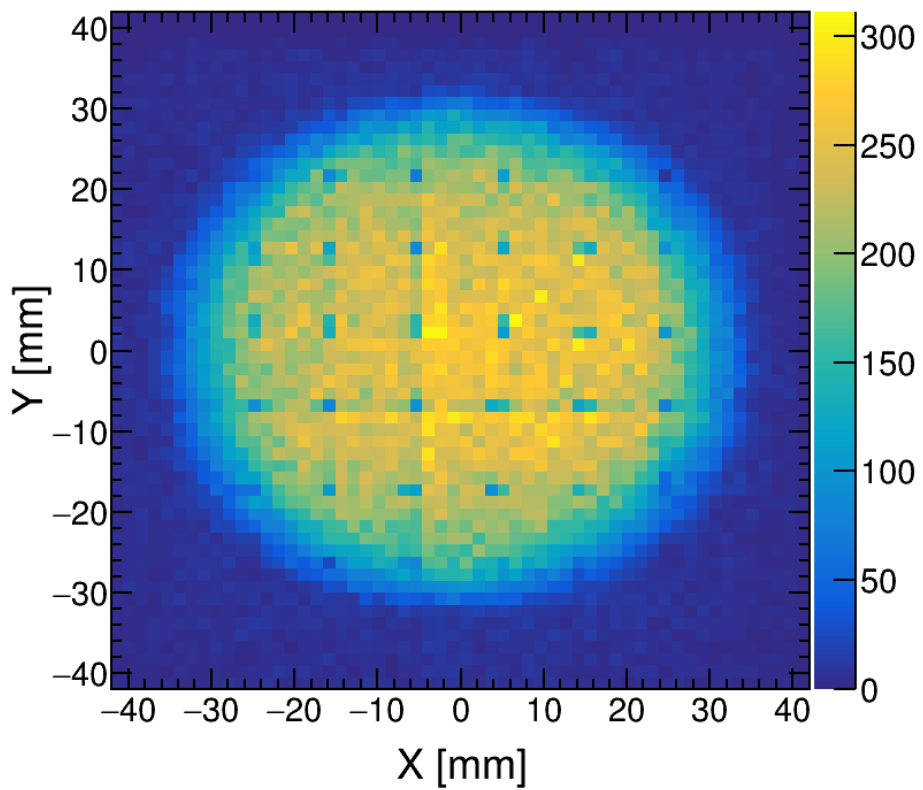


Figure 15: The reconstructed 2D profile of the Back-n white neutron beam at ES#1. The bin widths for the 2D histogram are 1.5 mm on both axes. The shaded dots in the profile image correspond to the reconstructed positions of the pillars.

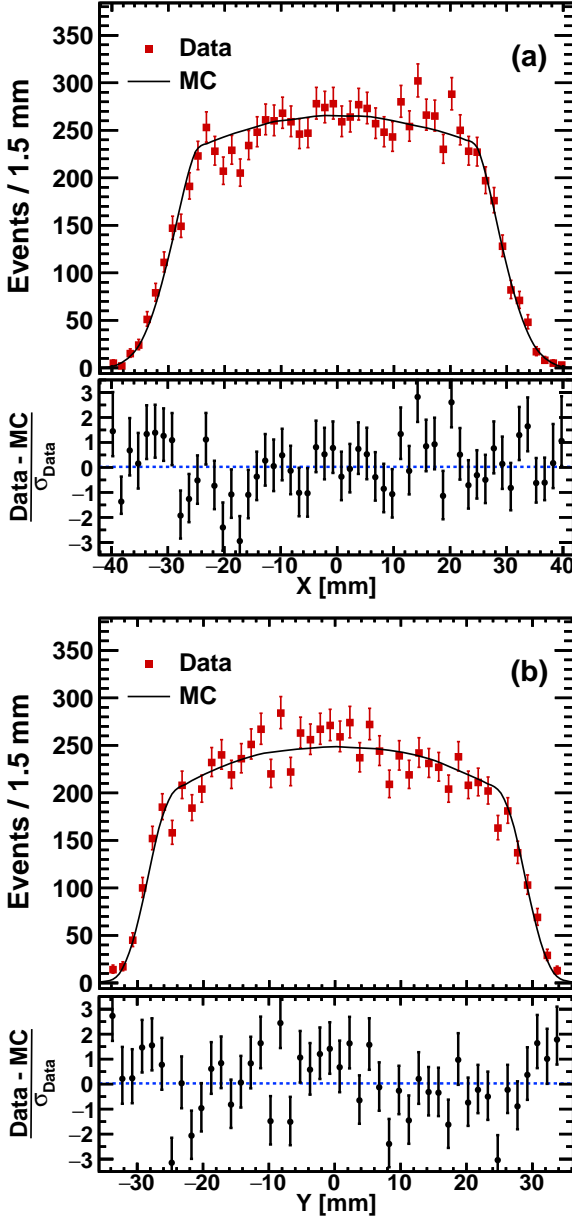


Figure 16: The upper panels show the 1D projections of (a) the middle Y-slice of the 2D beam profile onto the X-axis and (b) the middle X-slice of the 2D beam profile onto the Y-axis, for both data (solid squares) and MC simulation (solid curves). The expectation from the MC simulation is normalized to data. Each lower panel shows the significance of the deviation between the observed data and the simulation prediction in each bin of the distribution, considering only the statistical fluctuations in data.

5. Conclusions and outlook

Two variants of the 2D readout Micromegas-based neutron detector have been fabricated and characterized with an ^{55}Fe X-ray source, an ^{241}Am α source, and an Am-Be neutron source. The test results, including the relative electron transparency, the gain and the gain uniformity, and the neutron detection capability, showed that the detector performance meets the basic requirements for neutron beam profile measurement. Then, the neutron beam of the CSNS Back-n was measured and a 2D neutron beam spot distribution at the Back-n Endstation-1 was obtained. The good agreement between the simulations and experimental data confirms the reliability of this measurement.

The recording of the absolute time of the strip signal will be added in the front-end electronics configuration as part of the further development, such that (a) an online rejection of the γ -flash background and (b) measurement of the neutron TOF or energy spectrum will become possible. Other improvements will also be carried out, such as (a) increasing the length of the drift region to increase the strip multiplicity for a more precise determination of the neutron interaction point and (b) reducing the size of the pillars to reduce the neutron detection inefficiency caused by the pillars. Recently, the fabrication technique has been improved, reducing the diameter of the pillars to 0.5 mm.

6. Acknowledgements

This work was supported by National Key R&D Program of China (Grant No. 2016YFA0401600), National Natural Science Foundation of China (Grants No. 11605218 and No. 11605197), Fundamental Research Funds for the Central Universities, State Key Laboratory of Particle Detection and Electronics (Grants No. SKLPDE-ZZ-201801 and No. SKLPDE-ZZ-201818), and China Postdoctoral Science Foundation (Grant No. 2019M650845). This work was partially carried out at USTC Center for Micro- and Nanoscale Research and Fabrication, and we thank Yu Wei for his help on the nanofabrication steps for germanium coating.

References

- [1] H. T. Jing, et al., Studies of back-streaming white neutrons at CSNS, *Nucl. Instrum. Methods Phys. Res. A* 621 (1) (2010) 91–96.
- [2] J. Y. Tang, et al., Proposal for muon and white neutron sources at CSNS, *Chinese Phys. C* 34 (1) (2010) 121–125.
- [3] Q. An, et al., Back-n white neutron facility for nuclear data measurements at CSNS, *J. Instrum.* 12 (07) (2017) P07022–P07022.
- [4] H. S. Chen, X. L. Wang, China’s first pulsed neutron source, *Nat. Mater.* 15 (7) (2016) 689–691.
- [5] S. Wang, et al., Introduction to the overall physics design of CSNS accelerators, *Chinese Phys. C* 33 (S2) (2009) 1–3.
- [6] Y. Giomataris, P. Reboursard, J. P. Robert, G. Charpak, MICROMEGAS: a high-granularity position-sensitive gaseous detector for high particle-flux environments, *Nucl. Instrum. Methods Phys. Res. A* 376 (1) (1996) 29–35.
- [7] J. Pancin, et al., Measurement of the n_TOF beam profile with a micromegas detector, *Nucl. Instrum. Methods Phys. Res. A* 524 (1) (2004) 102–114.
- [8] M. Diakaki, et al., Development of a novel segmented mesh MicroMegas detector for neutron beam profiling, *Nucl. Instrum. Methods Phys. Res. A* 903 (2018) 46–55.
- [9] I. G. Irastorza, et al., Gaseous time projection chambers for rare event detection: results from the T-REX project. II. Dark matter, *J. Cosmol. Astropart. Phys.* 2016 (01) (2016) 034–034.
- [10] I. G. Irastorza, et al., Erratum: Gaseous time projection chambers for rare event detection: results from the T-REX project. II. Dark matter, *J. Cosmol. Astropart. Phys.* 2016 (05) (2016) E01–E01.

- [11] F. Belloni, F. Gunsing, T. Papaevangelou, Micromegas for neutron detection and imaging, *Mod. Phys. Lett. A* 28 (13) (2013) 1340023.
- [12] L. Guan, et al., Micromegas prototypes with thermo-bond film separators, *Chinese Phys. C* 35 (2) (2011) 163–168.
- [13] Z. Zhang, et al., Manufacture and performance of the thermal-bonding Micromegas prototype, *J. Instrum.* 9 (10) (2014) C10028–C10028.
- [14] C. Li, et al., Design of the FPGA-based gigabit serial link for PandaX-III prototype TPC, *Radiat. Detect. Technol. Methods* 1 (2) (2017) 25.
- [15] D. S. McGregor, et al., Design considerations for thin film coated semiconductor thermal neutron detectorsI: basics regarding alpha particle emitting neutron reactive films, *Nucl. Instrum. Methods Phys. Res. A* 500 (1) (2003) 272–308.
- [16] A. Badertscher, et al., First operation of a double phase LAr Large Electron Multiplier Time Projection Chamber with a 2D projective readout anode, *Nucl. Instrum. Methods Phys. Res. A* 641 (1) (2011) 48–57.
- [17] H. Kubo, et al., Development of a time projection chamber with micro-pixel electrodes, *Nucl. Instrum. Methods Phys. Res. A* 513 (1) (2003) 94–98, proceedings of the 6th International Conference on Position-Sensitive Detectors.
- [18] H. Nishimura, et al., The performance of the micro time projection chamber based on μ -PIC, in: 2006 IEEE Nuclear Science Symposium Conference Record, Vol. 6, 2006, pp. 3860–3864.
- [19] L. Y. Zhang, et al., Design of back-streaming white neutron beam line at CSNS, *Appl. Radiat. Isot.* 132 (2018) 212–221.
- [20] M. Iodice, Performance studies of MicroMegas for the ATLAS experiment, *J. Instrum.* 9 (01) (2014) C01017–C01017.